# Scale Size Estimation and Flow Pattern Recognition around a Magnetosheath Jet

Adrian Pöppelwerth[1], Georg Glebe[1,2], Johannes Z. D. Mieth[1], Florian Koller[3], Tomas Karlsson[4], Zoltan Vörös[5,6], and Ferdinand Plaschke[1]

[1]Institute of Geophysics and Extraterrestrial Physics, Technische Universität Braunschweig, Braunschweig, Germany
[2]School of Earth and Atmospheric Sciences, Georgia Institute of Technology, Atlanta, Georgia, USA
[3]Institute of Physics, University of Graz, Graz, Austria
[4]Division of Space and Plasma Physics, School of Electrical Engineering and Computer Science, KTH Royal Institute of Technology, Stockholm, Sweden
[5]Space Research Institute, Austrian Academy of Sciences, Graz, Austria
[6]Institute of Earth Physics and Space Science, HUN-REN, Sopron, Hungary

**Correspondence:** Adrian Pöppelwerth (a.poeppelwerth@tu-braunschweig.de)

**Abstract.** Transient enhancements in the dynamic pressure, so-called magnetosheath jets or simply jets, are abundantly found in the magnetosheath. They travel from the bow shock through the magnetosheath towards the magnetopause. On their way through the magnetosheath, jets disturb the ambient plasma. Multiple studies already investigated their scale size perpendicular to their propagation direction, and almost exclusively in a statistical manner. In this paper, we use multi-point measurements from the Time History of Events and Macroscale Interactions during Substorms (THEMIS) mission to study the passage of a single jet. We observe an vortical motion of the plasma on the jet path. Using this passage we can reconstruct the position of the central axis of this jet along its propagation direction. This method allows us to estimate the spatial distribution of the dynamic pressure within the jet. Furthermore, the size perpendicular to the propagation direction can be estimated for different cross sections. Using this method, the scale size of individual jet events can be determined with multiple spacecraft. In principle, only two spacecraft are needed if we assume a simplified geometry and stationarity of the jet during the observation.

In the jet event investigated here, both the dynamic pressure and the perpendicular size increase along the propagation axis from the front part towards the center of the jet and decrease again towards the rear part. We obtain a maximum diameter in the perpendicular direction of about 1 $R_{\mathrm{E}}$ and a dynamic pressure of about 6 nPa at the jet center.

## 1 Introduction

The magnetic field of the Earth is an obstacle to the supersonic solar wind. To flow around the magnetopause, the boundary between the terrestrial and interplanetary magnetic fields (IMF), the solar wind must be decelerated to sub-magnetosonic speeds. This takes place upstream at the bow shock where the solar wind is decelerated, heated and deflected.

Depending on the angle $\theta_{\mathrm{Bn}}$ between the bow shock normal and the IMF, the bow shock can be divided into a quasi-parallel ($\theta_{\mathrm{Bn}} < 45°$) or quasi-perpendicular ($\theta_{\mathrm{Bn}} > 45°$) shock (e.g., Balogh et al., 2005). Particles reflected at the quasi-parallel shock can travel far upstream along the IMF and interact with the incoming solar wind. This leads to a region called foreshock which

hosts a zoo of instabilities and waves (Eastwood et al., 2005). The waves are convected back to the shock with the solar wind, causing a rippled and undulated quasi-parallel bow shock.

The region between the bow shock and the magnetopause is called magnetosheath (e.g., Spreiter et al., 1966). In the magnetosheath, localized enhancements in the dynamic pressure are frequently observed. These so-called magnetosheath jets (see the review by Plaschke et al., 2018) were first reported by Němeček et al. (1998). Various definitions of jets can be found in the literature, which compare the dynamic pressure enhancement e.g. with the ambient plasma (e.g. Archer et al., 2012) or with the upstream solar wind (e.g. Plaschke et al., 2013). Jets are observed more often behind the quasi-parallel bow shock (e.g., Vuorinen et al., 2019) which corresponds to low IMF cone angle conditions for the subsolar magnetosheath and favor quiet solar wind (e.g., Plaschke et al., 2013). LaMoury et al. (2021) and Koller et al. (2023) further investigated the statistical dependence of jet occurrence on solar wind parameters. Jet impact rates determined by LaMoury et al. (2021) showed that more magnetosheath jets impact the magnetopause during low IMF magnitude, low solar wind density and high Mach number conditions. However, the dominant occurrence controlling parameters are low IMF cone angles and high solar wind speeds.

Jet formation downstream of the quasi-parallel bow shock may be explained by a mechanism suggested by Hietala et al. (2009, 2012). At the undulated bow shock, the incoming solar wind will be less decelerated and heated when passing the inclined parts. The geometry of the ripples can cause the flow to converge or diverge, resulting in density increases or decreases behind the shock. This leads to plasma regions with higher velocity and density than in the surrounding magnetosheath. Jets may also form due to solar wind discontinuities interacting with the bow shock (e.g., Archer et al., 2012). For example, Hot Flow Anomalies (HFAs, e.g. Savin et al., 2012) or short large amplitude magnetic structures (SLAMS, e.g. Schwartz and Burgess, 1991) can cause additional shock rippling when passing through the shock (e.g., Karlsson et al., 2018; Raptis et al., 2022b). That was also visible in simulations by Suni et al. (2021). They showed that jets can form due to the impact of compressional structures (like SLAMS) at the bow shock.

Geoeffective jets (with diameters $> 2R_\mathrm{E}$) reach the magnetopause several times per hour (Plaschke et al., 2020a) and have therefore a big impact on the magnetosphere and ionosphere. They can indent the magnetopause (e.g., Shue et al., 2009), cause surface waves (e.g., Archer et al., 2019) and may even penetrate through the boundary (e.g., Dmitriev and Suvorova, 2015). Hietala et al. (2018) showed that jets can trigger and suppress reconnection at the magnetopause, as they can modify the magnetic field in the magnetosheath and thus alter the shear angle at the magnetopause. This leads to situations where reconnection is triggered when it is not expected and vice versa (see also Vuorinen et al., 2021). Additionally, upon impact, jets can enhance ionospheric flow channels (Hietala et al., 2012) and disturb radio communication (Dmitriev and Suvorova, 2023). Nykyri et al. (2019) proposed that jets might even trigger substorms, leading to auroral brightenings. Also, Han et al. (2017) hypothesized in a statistical study that jets impacting the magnetopause are one possible source of throat auroras.

On their way from the bow shock to the magnetopause, plasma jets interact with the ambient magnetosheath plasma. Palmroth et al. (2021) used global hybrid-Vlasov simulations to study the evolution of jets inside the magnetosheath. They reported that the jets thermalize on their way to the magnetopause and become more 'magnetosheath-like' while they keep their propagation direction. In addition Raptis et al. (2022a) reported that jets may contain two plasma populations, a cold and fast jet and a hotter and slower background population. Not only the jets but also the ambient plasma is affected from the interaction.

Recent studies showed a slight alignment of the magnetic field along the jet propagation direction (Plaschke et al., 2020b) and a stirring of the magnetosheath plasma in the vicinity of the jet (Plaschke et al., 2017). Plaschke and Hietala (2018) reported in a statistical analysis that jets push slower plasma ahead of them and out of their way. Jets act like plows, and after their passage, the magnetosheath plasma fills the wake regions behind them. Plaschke and Hietala (2018) speculated that properties of jets like their scale size may influence the interaction.

Multiple studies report that magnetosheath jets have scale sizes in the order of 1 $R_{\mathrm{E}}$ in the directions parallel and perpendicular to the jet propagation. To obtain a simple estimation of the parallel size of a jet, it is sufficient to integrate the plasma velocity over the jet observation interval (Plaschke et al., 2020a) or multiply the duration of the jet interval with the maximum speed to get an upper size limit (Gunell et al., 2014). To obtain the perpendicular size at least two spacecraft are needed. Plaschke et al. (2016, 2020a) and Gunell et al. (2014) used pairs of spacecraft and derived the scale sizes in statistical studies from the probabilities for both spacecraft to observe a jet. Karlsson et al. (2012) used the four Cluster spacecraft (Escoubet et al., 2001) to investigate the scale sizes of single jets. The authors performed a minimum variance analysis to obtain a suitable, jet specific coordinate system. They extrapolated density profiles along these directions with linear fits allowing them to estimate the scale sizes in all 3 directions.

However, apart from Karlsson et al. (2012), all aforementioned authors used statistical analyses to obtain information on the scale sizes and other properties of magnetosheath jets. Here we show for the first time the spatial distribution of the dynamic pressure within different cross sections of a jet. To achieve this, we select a jet event observed by the Time History of Events and Macroscale Interactions during Substorms (THEMIS) spacecraft (Angelopoulos, 2008) and transform the velocity measurements in to a coordinate system aligned with the jet propagation direction. We use the vortical behavior of the plasma in the jet path (Plaschke and Hietala, 2018) to determine the position of the spacecraft within the plane perpendicular to the propagation direction. Ultimately, we use the positions and measurements of the spacecraft to estimate dynamic pressure profiles perpendicular to the propagation direction within different cross sections. In addition, we determine the perpendicular sizes with these profiles for different cross sections.

## 2 Data and Methods

We focus on a jet observed by the THEMIS A, D, and E spacecraft (THA, THD, THE) on 13 October 2010, around 16:04:00 UT. Measurements of the magnetic field (FGM, Auster et al., 2008), ion velocity, ion density, ion energy flux density and dynamic pressure (ESA, McFadden et al., 2008) in the GSE-X direction ($P_{\mathrm{dyn,x}}$) are shown in Fig. 1 in the rows from top to bottom (full moments in spin resolution). Following Plaschke et al. (2013), we label the point of maximum dynamic pressure ratio with reference to the upstream OMNI solar wind measurements (King and Papitashvili, 2005) as $t_{\mathrm{max}}$. Start and end times of the jet interval are labeled as $t_{\mathrm{start}}$ and $t_{\mathrm{end}}$, respectively. They denote the times where $P_{\mathrm{dyn,x}}$ equal one quarter of the solar wind dynamic pressure ($P_{\mathrm{dyn,sw}}$). The spacecraft THA, THD and THE observed the jet for 50 s, 66 s and 43 s, respectively.

The ion energy flux density (Fig. 1a4-c4) together with the high ion density (Fig. 1a3-c3) clearly show that all three spacecraft are in the magnetosheath at the time of the event. The positions in GSE coordinates are given above each column of the figure;
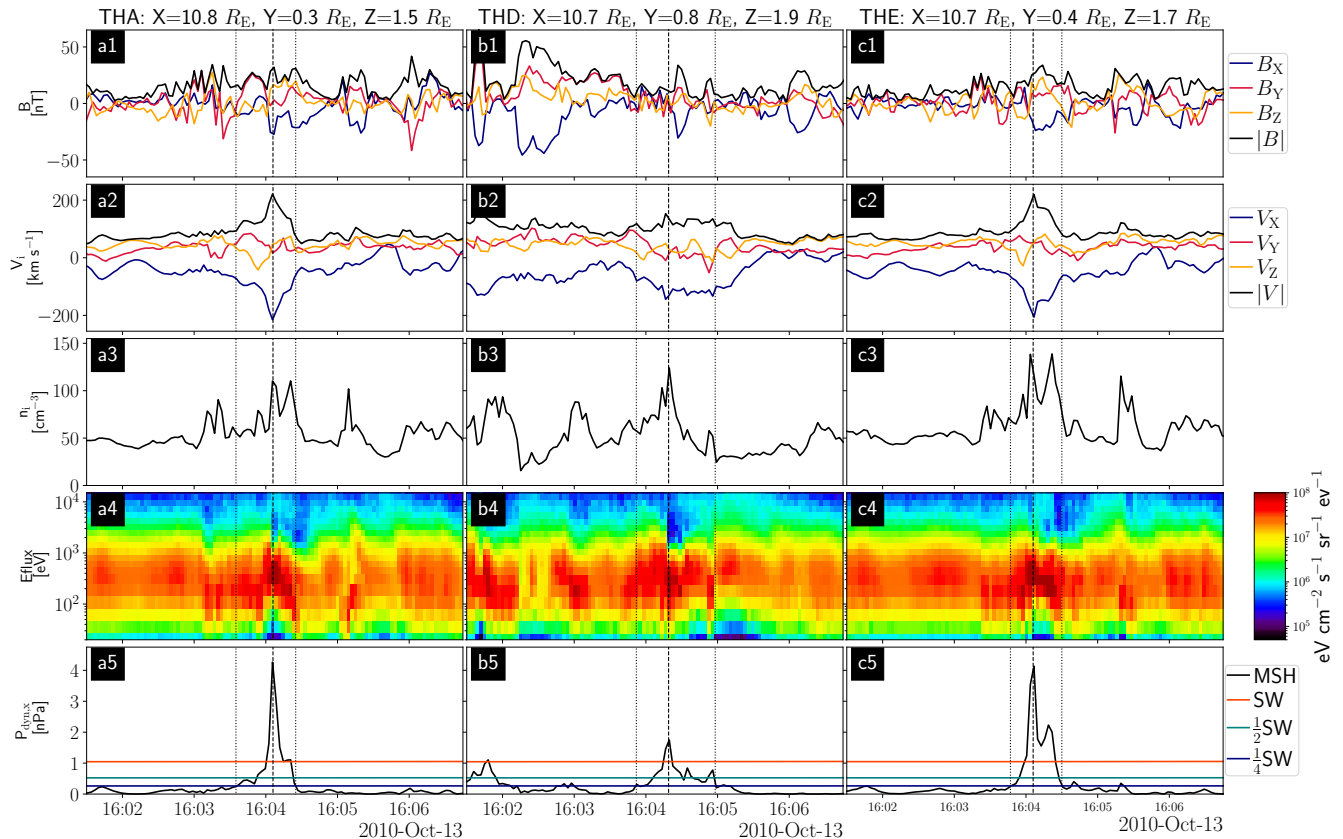
**Figure 1.** Plasma jet observed by the three THEMIS spacecraft THA (a), THD (b), and THE (c), respectively. From top to bottom, the magnetic field and ion velocity components in GSE coordinates and their magnitudes, the ion density, the ion energy flux density, and the GSE-X component of the dynamic pressure are shown. The vertical dashed lines in each column mark the times of maximum dynamic pressure ratio ($t_{\mathrm{max}}$). The dotted lines denote the start ($t_{\mathrm{start}}$) and end times ($t_{\mathrm{end}}$) of the jet intervals. The horizontal lines in the last row represent the solar wind dynamic pressure, as well as half and a quarter thereof (in orange, cyan, and blue, respectively).

they show that all spacecraft are close to the sun-earth line. The dynamic pressure (Fig. 1a5-c5) exhibits a clear increase above
90  the solar wind value for all spacecraft, ensuring that we are indeed observing a jet. The times $t_{\mathrm{max}}$ are separated by only 13 s and the dynamic pressure peaks resulted from a combined increase in ion density and $V_{\mathrm{x}}$ for every spacecraft.

Raptis et al. (2022a) have shown by investigating the velocity distribution function (VDF) that jets may contain a mixture of two plasma populations. In a similar manner we integrated the 3D VDF over two velocity axes to obtain a 1D VDF along the third velocity component. This is shown in Fig. 2 for time $t_{\mathrm{max}}$ for all three velocity components of THA, THD and THE.

95  We notice in agreement with Raptis et al. (2022a) that the $V_{\mathrm{y}}$ component (VDF) of THD (see Fig. 2b2) shows two separate maxima. THA and THE measurements exhibit only single peaks in the 1D VDFs, but deviate from the ideal Maxwellian distribution (see Fig. 2a1-a3 and c1-c3). As THD is further away from the other two spacecraft and observes a lower dynamic
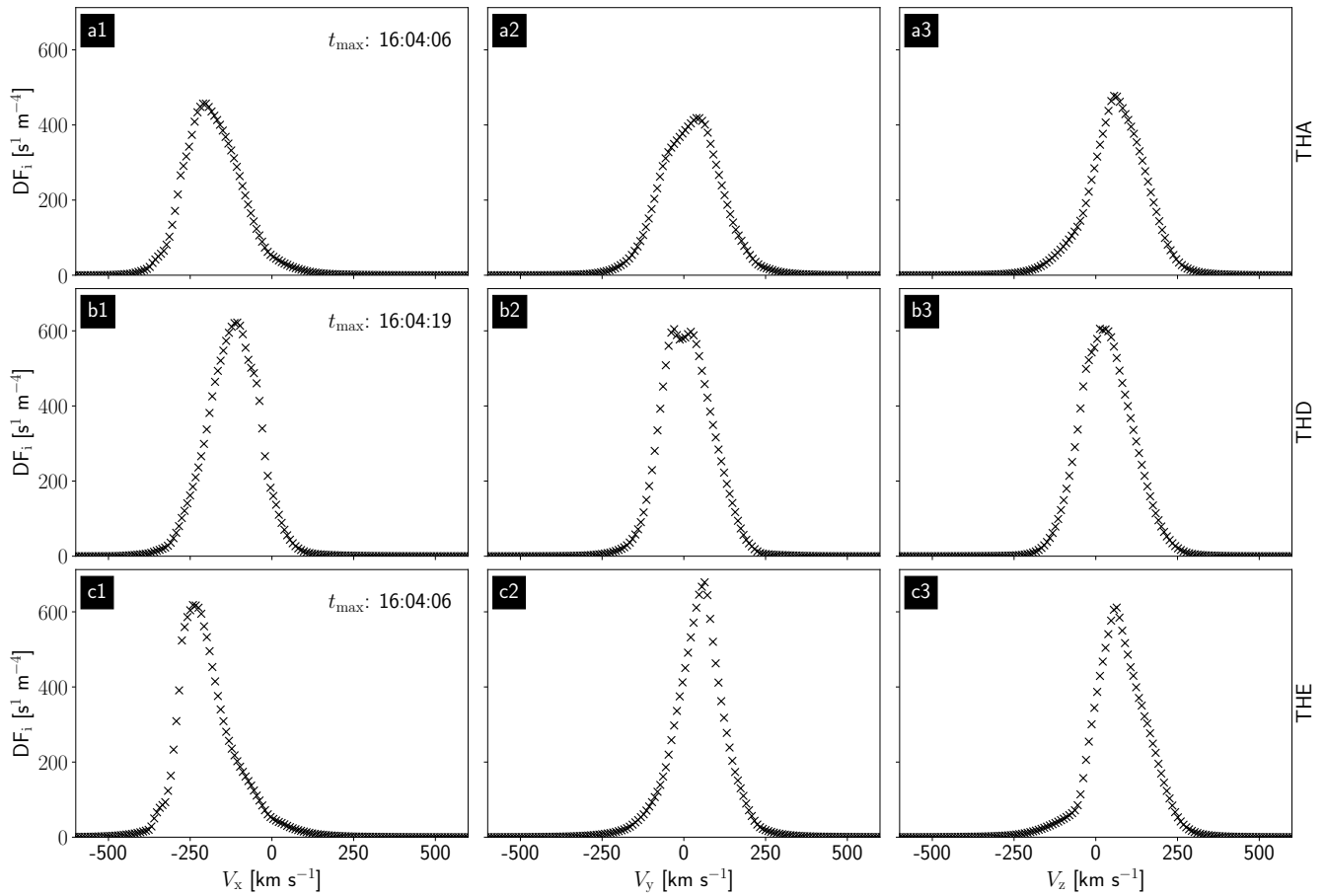
**Figure 2.** The integrated 1D velocity distribution function along the velocity components at the time of maximum dynamic pressure $t_{\mathrm{max}}$. The columns from left to right represent the $V_{\mathrm{x}}$, $V_{\mathrm{y}}$ and $V_{\mathrm{z}}$ component, respectively. The rows from top to bottom show the results for THA, THD and THE, respectively. In the left column we denote the time $t_{\mathrm{max}}$ for each spacecraft.

pressure, we assume THD to be closer to the edge of the jet. The two maxima could indicate that THD is observing a mixture of jet and magnetosheath plasmas. Therefore, we continue our analysis only considering THA and THE, using the peak velocities in the 1D VDFs.

To facilitate the analysis of the measurements, we need to define a coordinate system that is aligned with the direction of the jet propagation. As apparent in Fig. 1 the velocities are rather turbulent. Therefore, we choose a short time (12 s) centered around $t_{\mathrm{max}}$ and investigated the velocity directions measured by THA and THE to determine the propagation direction. For an easier comparison of the directions we use spherical coordinates with the polar angle $\Theta$ and the azimuthal angle $\varphi$ to visualize the direction of the velocities:

$$\Theta = \arccos\left(\frac{z}{\sqrt{x^2 + y^2 + z^2}}\right), \quad \varphi = \mathrm{sgn(y)} \cdot \arccos\left(\frac{x}{\sqrt{x^2 + y^2}}\right). \tag{1}$$
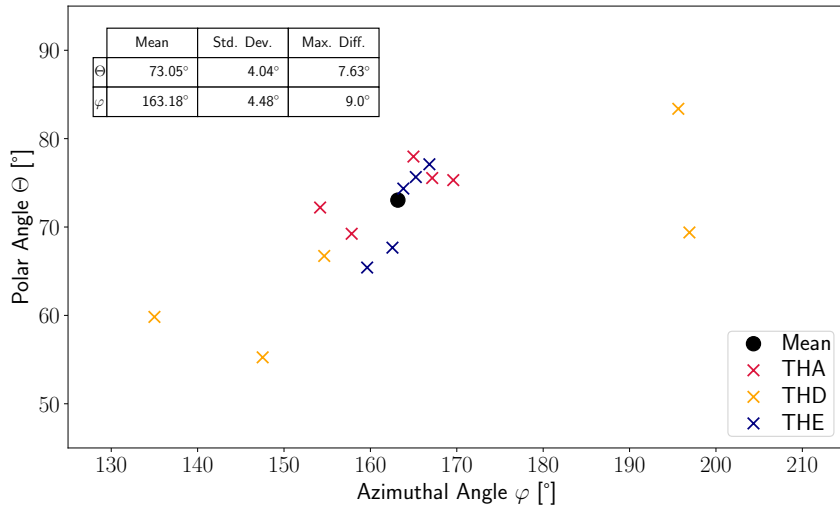
**Figure 3.** The polar angle $\Theta$ plotted against the azimuthal angle $\varphi$ for velocity measurements of THA, THD and THE around $t_{\mathrm{max}}$ in red, orange and blue, respectively. The black dot represents the mean value of the THA and THE measurements. The table in the upper right shows the mean values, standard deviations and maximum differences of $\Theta$ and $\varphi$.

The results are shown in Fig. 3 where the crosses in red, orange and blue represent the measurements of THA, THD and THE, respectively. THD is deviating strongly from THA and THE and is only shown for completeness. The black dot represents the mean value of the THA and THE measurements.

110      The directions of THA and THE are more similar and variate not to much around $t_{\mathrm{max}}$. We therefore can assume that the mean values of $\Theta = 73.05°$ and $\varphi = 163.18°$ represent the propagation direction $V_{\mathbf{jet}}$ well. In addition, we also calculate the standard deviation ($\Theta = 4.04°, \varphi = 4.48°$) and maximum difference from the mean ($\Theta = 7.63°, \varphi = 9.00°$). To treat the uncertainty of the propagation direction conservatively, we will use the maximum differences as error estimation. With the mean values for $\Theta$ and $\varphi$ we determine the propagation direction $V_{\mathbf{jet}} = [-0.92, 0.28, 0.29]$ (in GSE coordinates) and calculate

115 the axes of the new coordinate system as follows:

$$X' = V_{\mathbf{jet}}, \quad Y' = \frac{X' \times \hat{X}}{|X' \times \hat{X}|}, \quad Z' = \frac{X' \times Y'}{|X' \times Y'|}. \tag{2}$$

$\hat{X}$ is the unit vector along the GSE-X axis. $X'$ points in the propagation direction of the jet, while $Y'$ and $Z'$ are oriented perpendicular to the propagation direction and complete the right handed system. We choose the position of spacecraft THA at $t_{\mathrm{max}}$ (see Fig. 1) as origin of our jet coordinate system since THA observes the highest dynamic pressure. To transform the

120 velocities and positions we simply rotate them into the new coordinate system.

     Using the jet coordinate system, we can investigate the flow patterns at the spacecraft positions. This is shown in Fig. 4, where the arrows indicate the ion velocities at the spacecraft positions (circles) of THA, THD and THE in red, orange and blue, respectively. The figure shows the orientation of the velocities in the $Y' - Z'$ plane, perpendicular to the propagation direction, for 11 time steps from 15 s before to 15 s after $t_{\mathrm{max}}$. The $Y'$- and $Z'$-axis are identical for each time step.
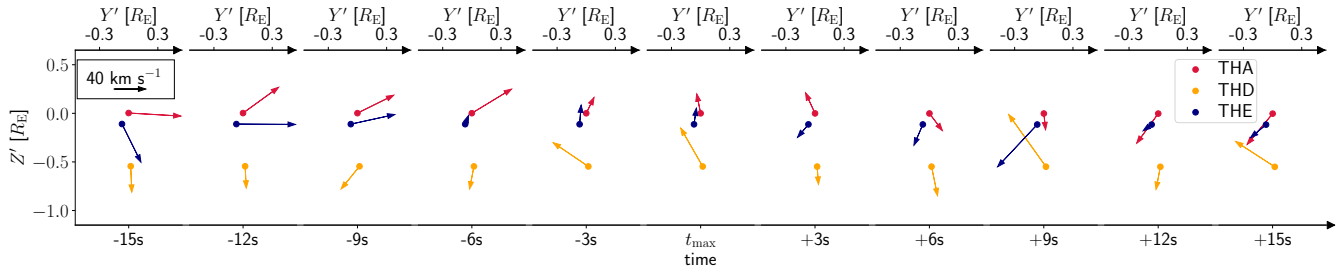
**Figure 4.** Ion velocities from the 1D VDF peaks at the three spacecraft positions for 11 time steps around $t_{\mathrm{max}}$ in the plane perpendicular to the jet propagation direction. The circles represent the spacecraft positions and the arrows indicate the velocities. The colors for THA, THD, and THE are red, orange, and blue, respectively. The top axis shows the corresponding $Y'$ coordinates for each time step, while the bottom axis displays the time steps. In the upper left corner, the black arrow indicates the scale.

125     Plaschke and Hietala (2018) have reported that the vortical motion of the plasma is not only visible outside of the jet but is also apparent within the jet structure. Therefore we choose this time range where all spacecraft observe the jet. We remind the reader that we will primarily focus on THA and THE as we have already discussed that THD is further away from the other two spacecraft and might observes a mixture of plasma populations. This said, we argue that the following description applies also to THD but we expect deviations from the general behavior as the conditions are different compared with THA and THE.

130     On the left side of Fig. 4, prior to $t_{\mathrm{max}}$, the arrows point towards the positive $Y'$ direction, but in different $Z'$ directions. We interpret this as signs of diverging flow. Closer to $t_{\mathrm{max}}$, from 3 s before to 9 s after $t_{\mathrm{max}}$, the arrows show a rather turbulent behavior and we observe rotations of the arrows, mostly in counterclockwise direction. Looking at Fig. 1a5 and c5 we see two high dynamic pressure peaks in this time interval at THA and THE. In contrast, the arrows on the right side in Fig. 4, from -12 s to -15 s, corresponding with times after $t_{\mathrm{max}}$, point towards the negative $Y'$ direction. The arrows point additionally to

135 roughly one point and show signs of a converging plasma flows.

    In Appendix A we show that the visibility of this vortical motion is not strongly dependent on the propagation direction, as the same flow patterns are still visible at THA and THE for slightly rotated coordinate systems that are consistent with the determined uncertainties.

    Next we determine which regions of the jet the spacecraft observe. In order to achieve this, we use the diverging flows

140 before and the converging flows after $t_{\mathrm{max}}$ to estimate the position of the central axis of the jet. Thereafter, we can calculate the spacecraft distances from the central axis within different cross sections of the jet.

    We extend the THA- and THE- velocity vectors in the $Y'$-$Z'$-plane and determine the central axis as the point where the two lines intersect. As an example, in Fig. 5a, b we show the estimation for the time steps 12 s before and 15 s after $t_{\mathrm{max}}$. The gray lines indicate the extension of the velocity vectors and the black cross represents the estimated position of the central axis.

145 In Fig. 5c we present the estimated positions of the central axis for all time steps, except where we observe the largest dynamic pressures (from 3 s before to 9 s after $t_{\mathrm{max}}$).
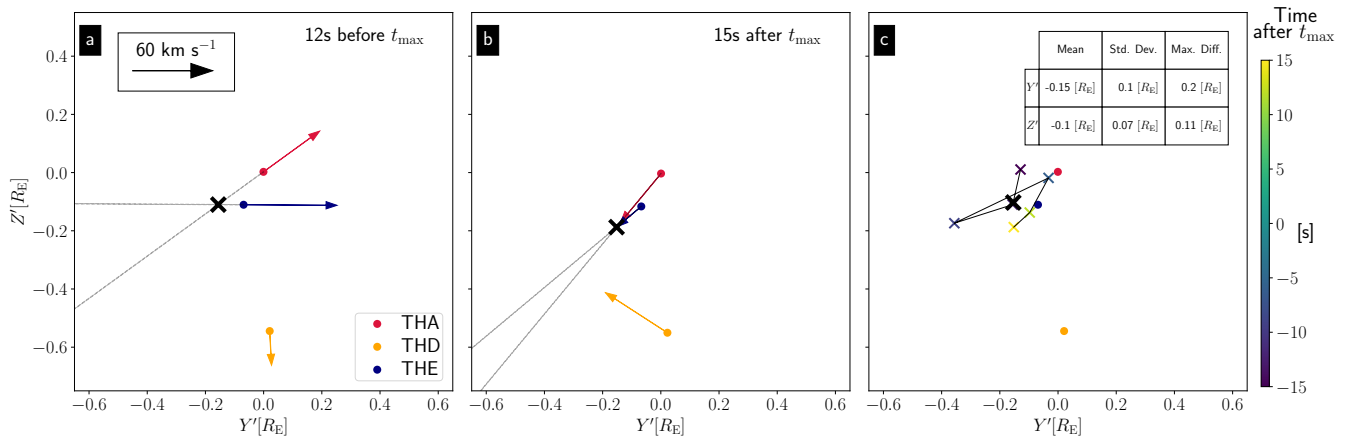
**Figure 5.** a) and b): Ion velocities from 1D VDF peaks at the three spacecraft positions 12 s before (a) and 15 s after $t_{max}$ (b) in the plane perpendicular to the jet propagation. The circles represent the positions of the spacecraft and the arrows indicate the velocities. The colors for THA, THD, and THE are red, orange, and blue, respectively. The black arrow indicates the scale. The gray lines are simple extensions of the velocity vectors, and the black crosses mark the intersections of the lines, and representing the estimated center positions. c): The colored crosses show the estimated positions for different time steps. The color corresponds to the time as indicated by the color bar. The black cross represents the mean value and the dots in red, orange and blue are the positions of THA, THD and THE, respectively. The table in the upper right denotes the mean values, standard deviations and maximum differences of the $Y'$ and $Z'$ coordinates.

Based on Fig. 5c, we can calculate the mean position of the central axis: $Y' = 0.15 \ R_E$ and $Z' = 0.10 \ R_E$. We also observe that the position is relatively well determined, as can be seen by the low standard deviations ($Y' = 0.10 \ R_E$, $Z' = 0.07 \ R_E$) and maximum differences ($Y' = 0.20 \ R_E$, $Z' = 0.11 \ R_E$). Only the estimation at -9 s causes a large error, especially in the $Y'$

150  direction. Again, to be conservative, we use the maximum differences as uncertainties and assume the position of the central axis to be valid for the entire jet interval.

In the next section we will use the spacecraft positions and their distances from the central axis to investigate the dynamic pressure profiles for different cross sections. In order to achieve this, we fit a Gaussian distribution that also can be used to estimate the scale size of the corresponding cross section to the $P_{dyn}$ measurements:

$$155 \quad P_{\text{dyn,fit}} = P_0 \cdot \exp\left(\frac{-r^2}{2 \cdot \Delta R^2}\right). \tag{3}$$

Here the parameters $P_0$ and $\Delta R$ are the amplitude and width of the Gaussian, and $r$ represents the distance to the center. The choice of the Gaussian profile may be somewhat arbitrary. Even though we cannot guarantee that it describes the jets in reality, the measurements in this case are well described by this profile. To apply this fit we have to assume a monotonous decrease of the dynamic pressure from the center towards the edges. We furthermore assume a rotational symmetry around the central jet

160  axis to ensure a robust fit.
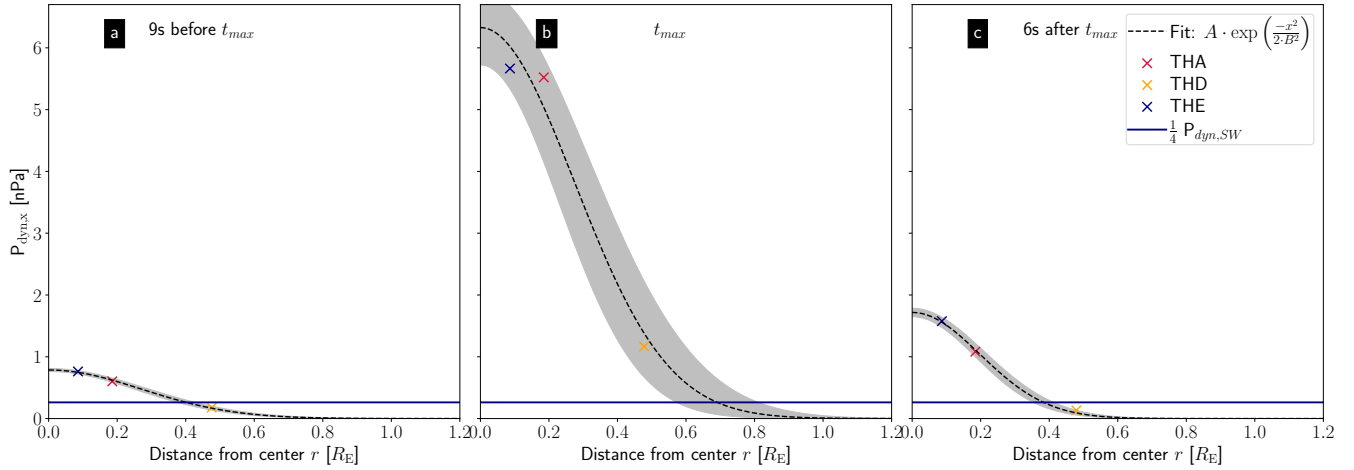
**Figure 6.** Dynamic pressure $P_{\mathrm{dyn,x}}$ derived from velocities from the 1D VDFs in the spacecraft system versus the distance from the center $r$ at THA, THD and THE (crosses in red, orange and blue, respectively) at 9 s before $t_{\max}$ (a), at $t_{\max}$ (b) and at 6 s after $t_{\max}$ (c). The black, dashed line represent a fit with a Gaussian distribution to the data points and the gray area visualizes when we subtract/add one standard deviation $\sigma$ from the optimal fit parameters. The blue horizontal line depicts a quarter of the solar wind dynamic pressure.

## 3 Results and Discussion

Using the estimated position of the central axis, we calculate the distances of the spacecraft from the central axis $r$ in the $\boldsymbol{Y'}$-$\boldsymbol{Z'}$-plane. This results in distances of 0.19 $R_{\mathrm{E}}$, 0.48 $R_{\mathrm{E}}$ and 0.09 $R_{\mathrm{E}}$ for THA, THD and THE, respectively. These values change only marginally (max. 3%) over the jet interval due to the spacecraft movement, assuming the central axis staying
165  constant.

To obtain dynamic pressure profiles we, plot $P_{\mathrm{dyn,x}}$ derived from peak velocities from the 1D VDFs in the spacecraft system against these distances for different times and apply the Gaussian fit. In Fig.6 we show this for the times $t_{\max}-9$ s (a), $t_{\max}$ (b) and $t_{\max}+6$ s (c). Crosses in red, orange, and blue represent the data points for THA, THD and THE, respectively. We also plot one quarter of the solar wind dynamic pressure (blue horizontal line) in Fig.6 and the Gaussian distribution is shown as
170  black dashed line. The gray area visualizes the standard deviation $\sigma$ of the optimal fit parameters. Here, $\sigma$ is the square root of the diagonal elements of the covariance matrix for the fitting parameters.

In the three time steps shown, the dynamic pressure is highest at the spacecraft closest to the center (THE). While we see some deviations from the data in Fig.6b (larger gray area), the fit in Fig.6a and c represents the data points very well. The fit parameters are $P_0 = 0.79 \pm 0.02$ nPa and $\Delta R = 0.28 \pm 0.01$ $R_{\mathrm{E}}$ at $t_{\max}-9$s, $P_0 = 6.33 \pm 0.60$ nPa and $\Delta R = 0.28 \pm 0.04$ $R_{\mathrm{E}}$
175  at $t_{\max}$ and $P_0 = 1.72 \pm 0.07$ nPa and $\Delta R = 0.20 \pm 0.01$ $R_{\mathrm{E}}$ at $t_{\max}+6$s. The estimated central jet dynamic pressure is higher at $t_{\max}$ (6 nPa) than earlier at $t_{\max}$-9s (1 nPa) or later at $t_{\max}+6$s (2 nPa). Hence, the dynamic pressure increases along the central jet axis from the front part towards the center of the jet and decreases afterwards towards the rear part.

The intersection of the fit with $P_{\text{dyn,x}} = \frac{1}{4} P_{\text{dyn,sw}}$ =0.26 nPa leads to an estimation of the jet size in the direction perpendicular to the jet propagation. We choose one quarter of the solar wind dynamic pressure as a threshold to be consistent with the definition of $t_{\text{start}}$ and $t_{\text{end}}$ for jets, which determine the scale size along the jet propagation direction (see criterion of Plaschke et al., 2013). The Gaussian fits (black lines) intersect the horizontal line at 0.39 $R_{\text{E}}$, 0.68 $R_{\text{E}}$ and 0.38 $R_{\text{E}}$ at $t_{\text{max}}-9$ s, $t_{\text{max}}$ and $t_{\text{max}}+6$ s, respectively. As the width of the Gaussian distribution $\Delta R$ is quite similar in all three time steps, the larger (smaller) perpendicular size of the jet around $t_{\text{max}}$ ($t_{\text{max}}$-9 s and $t_{\text{max}}$+6 s) results from the higher (lower) dynamic pressure in the jet center (front and rear parts).

We apply the fit here to the measurements from all three spacecraft to reduce the uncertainty of the parameters. In Appendix B we show that the dynamic pressure profiles do not strongly depend on the position of the central axis, as the parameters $P_0$ and $\Delta R$ and their evolution over the jet interval vary only marginally with varying central axis position.

We can compare the estimated scale sizes with previous results. In previous studies, different authors reported a range of scale sizes of magnetosheath jets. Plaschke et al. (2020a) derived that most of the jets should be on the order of 0.1 $R_{\text{E}}$, although they argued that these small jets are less likely to be observed. For the observed magnetosheath jets, they report a median diameter of about 1 $R_{\text{E}}$ in the directions parallel and perpendicular to the flow. Gunell et al. (2014) calculated upper limits and found median values of 4.9 $R_{\text{E}}$ and 3.6 $R_{\text{E}}$ for the sizes parallel and perpendicular to the flow, respectively. Both studies used pairs of spacecraft and the probabilities that both observe a jet to calculate sizes perpendicular to the propagation directions. Karlsson et al. (2012) found scale sizes between 0.1 and 10 $R_{\text{E}}$ for one direction perpendicular to the magnetic field; for the other two dimensions the sizes were found to be a factor of 3-10 larger. Thus our results with diameters of approximately 1.3 $R_{\text{E}}$ at $t_{\text{max}}$ and 0.8 $R_{\text{E}}$ at times before and after $t_{\text{max}}$ fit very well to the earlier reported sizes.

The method presented by Karlsson et al. (2012) can be used to obtain the sizes of single jets in all three dimensions. This is only possible if the structure is associated with a magnetic field discontinuity, which was the case for all their events. Contrary to this, our method provides scale sizes for the directions parallel and perpendicular to the flow under the assumption of rotational symmetry and a constant propagation direction. We have shown that the latter is given for this jet event to some extent. Furthermore, we assume radial dynamic pressure profiles that resemble Gaussian distributions. The problem can thus be reduced to two dimensions. This enables us estimate the perpendicular scale size for different cross sections of a jet. Together with the parallel scale size, we could create a simple 3D model of the magnetosheath jet. To apply this method, it is necessary to observe the flow pattern described by Plaschke and Hietala (2018). At least one of the two motions - diverging or converging plasma flow - should be visible to determine the position of the jet central axis. Observing both parts of the vortical motion leads to more reliable results. This estimation is therefore not applicable to all jets observed by multiple spacecraft, as individual events can deviate strongly from the average behavior. As Plaschke et al. (2020b) have shown for the alignment of velocity and magnetic field, the fluctuations can easily be on the same order of magnitude as the average alignment effect.

Note that the method described in this paper relies on above mentioned assumptions and simplifications. The choice of the Gaussian distribution for the fit implies a corresponding monotonous decrease of the dynamic pressure from the center towards the edges. These assumptions may not necessarily be satisfied in general or in some parts of the jet. To perform our analysis we need at least two spacecraft. However, as evident for this jet event, this is not necessarily sufficient, as the spacecraft should

be well separated from each other. More spacecraft observing the same jet or the ambient magnetosheath would allow an evaluation of the validity of our assumptions.

## 4 Summary and Conclusion

We observed the vortical motion of plasma within a jet with the three THEMIS spacecraft THA, THD and THE. From the diverging flows ahead of and the converging plasma flows behind the jets maximum dynamic pressure region (at $t_{\mathrm{max}}$) we were able to estimate the position of the jet central axis. The distances of the spacecraft from the central axis were used together with the measured $P_{\mathrm{dyn,x}}$ to fit Gaussian distributions. This allowed us to determine the dynamic pressure profiles and the perpendicular sizes of the jet within different cross sections.

Here we demonstrate a new method to determine the size for single jet events using in principle measurments from only two spacecraft. In this paper, dynamic pressure profiles for the jet event were presented for three different times ($t_{\mathrm{max}}$-9 s, $t_{\mathrm{max}}$ and $t_{\mathrm{max}}$+6 s) with the following two results:

1. The dynamic pressure in the central part of the jet is higher at $t_{\mathrm{max}}$ (6 nPa) and decreases towards the front and rear parts,

2. The width of the Gaussian distribution is rather constant over the jet interval. This results in a larger perpendicular size at $t_{\mathrm{max}}$ (1.2 $R_{\mathrm{E}}$) due to the higher dynamic pressure in the center.

The apparent larger scale size around $t_{\mathrm{max}}$ suggests that some spacecraft may only observe central parts of a jet rather than the front and rear parts when passing through edge regions. In addition, spacecraft will unlikely observe the exact center of a jet. Thus, they would measure just a fraction of the dynamic pressure in the jet center (a lower limit) as $P_{\mathrm{dyn,x}}$ decreases towards the edges and this would not necessarily be representative for the jet. This implies that statistical studies of dynamic pressures of jets may significantly and systematically underestimate the maximum values (e.g., Raptis et al., 2020).

The jet event selected for this case study belongs to a fraction of jet observations that show signs of the expected flow pattern that is needed for the estimation of the center. With only three spacecraft available, there are uncertainties regarding the quality and applicability of the fit and validity of our assumption of rotational symmetry. To increase our confidence in the fit and our assumptions, it would be useful to obtain measurements from even more spacecraft on a jet. This could be achieved through conjunctions of spacecraft from different missions like Cluster, Magnetospheric Multiscale (MMS, Burch et al., 2016) and THEMIS.

### Appendix A: Uncertainty of $V_{\mathbf{jet}}$

The propagation direction of the jet ($V_{\mathbf{jet}}$) may have a great impact on our analysis. If the direction is incorrect or poorly determined, it is possible that we do not notice the vortical movement even though it is actually present or vice versa. We estimated $V_{\mathbf{jet}}$ as a mean value of multiple measurements by THA and THE. Thus, we imply a constant propagation direction
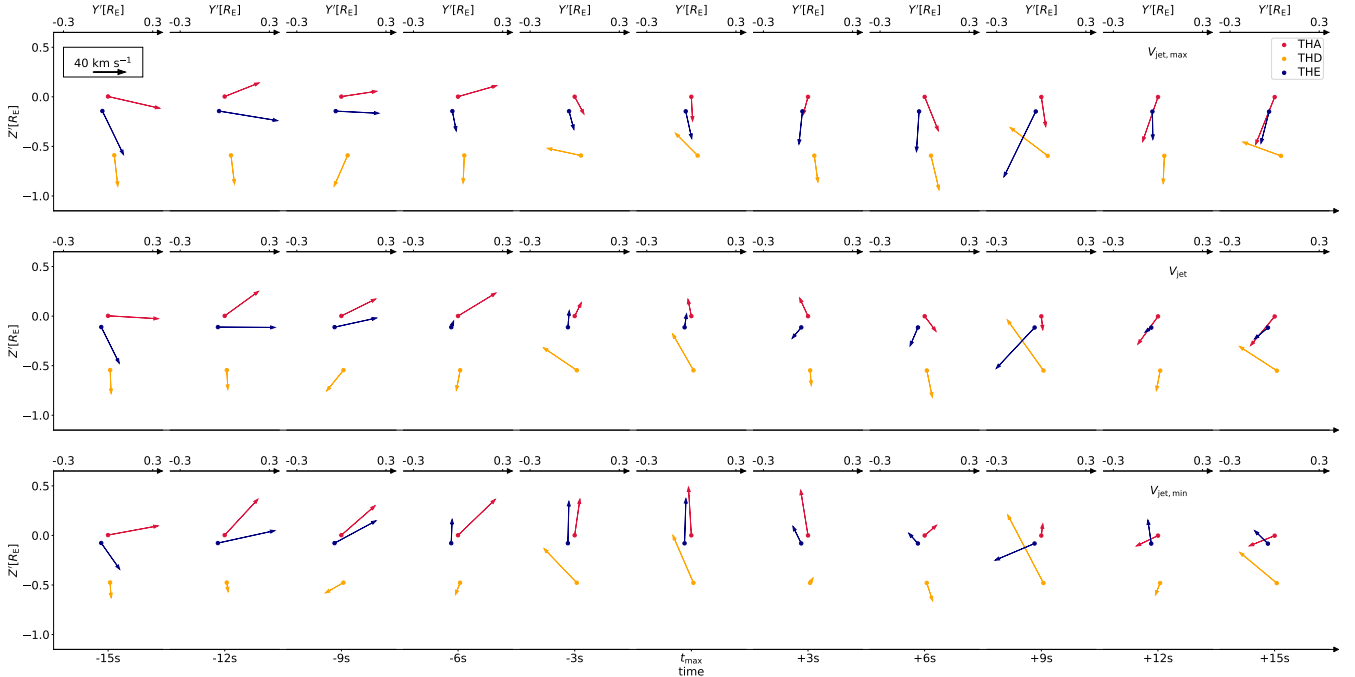
**Figure A1.** Ion velocities from the 1D VDF peaks at the three spacecraft positions for 11 time steps around $t_{\mathrm{max}}$ in the plane perpendicular to the jet propagation direction. The circles represent the spacecraft positions and the arrows indicate the velocities. The colors for THA, THD, and THE are red, orange, and blue, respectively. The top axes show the corresponding $\boldsymbol{Y}'$ coordinates for each time step, while the bottom axes display the time steps. In the upper left corner, the black arrow indicates the scale. The top, middle and bottom row were calculated with $\boldsymbol{V}_{\mathrm{jet,max}}$, $\boldsymbol{V}_{\mathrm{jet}}$ and $\boldsymbol{V}_{\mathrm{jet,min}}$ as propagation direction, respectively.

over time and that the velocities at both spacecraft positions represent the propagation well. To handle the uncertainty of this assumptions, we take a look at the maximum differences from the mean velocity (cf. Fig. 3). Adding or subtracting these values

245    to/from $\boldsymbol{V}_{\mathrm{jet}}$ result in $\boldsymbol{V}_{\mathrm{jet,max}}$ and $\boldsymbol{V}_{\mathrm{jet,min}}$ as alternative propagation directions.

With $\boldsymbol{V}_{\mathrm{jet,max}}$ and $\boldsymbol{V}_{\mathrm{jet,min}}$ we can transform the measured ion velocities and the positions of the spacecraft into new coordinate systems using Eq. 2. We than look at the transformed velocities in the $\boldsymbol{Y}' - \boldsymbol{Z}'$ plane (perpendicular to the propagation direction). This is shown in Fig. A1 for $\boldsymbol{V}_{\mathrm{jet,max}}$ in the top row, for $\boldsymbol{V}_{\mathrm{jet,min}}$ in the bottom row and for $\boldsymbol{V}_{\mathrm{jet}}$ in the middle row (for comparison).

250    We observe the diverging flows before and the converging flows after $t_{\mathrm{max}}$ in all three cases. In addition, we also investigate if the use of the peak velocities of the 1D VDFs has an influence on our results. Therefore we use the same propagation directions $\boldsymbol{V}_{\mathrm{jet,max}}$, $\boldsymbol{V}_{\mathrm{jet}}$ and $\boldsymbol{V}_{\mathrm{jet,min}}$ and transform the ion velocities calculated from the full moments. This is shown in Fig. A2.

Although there are some changes, we can again observe in all cases the diverging flows before and the converging flows

255    after $t_{\mathrm{max}}$. Thus we conclude that the flow pattern we observe is not an artifact from our data handling.
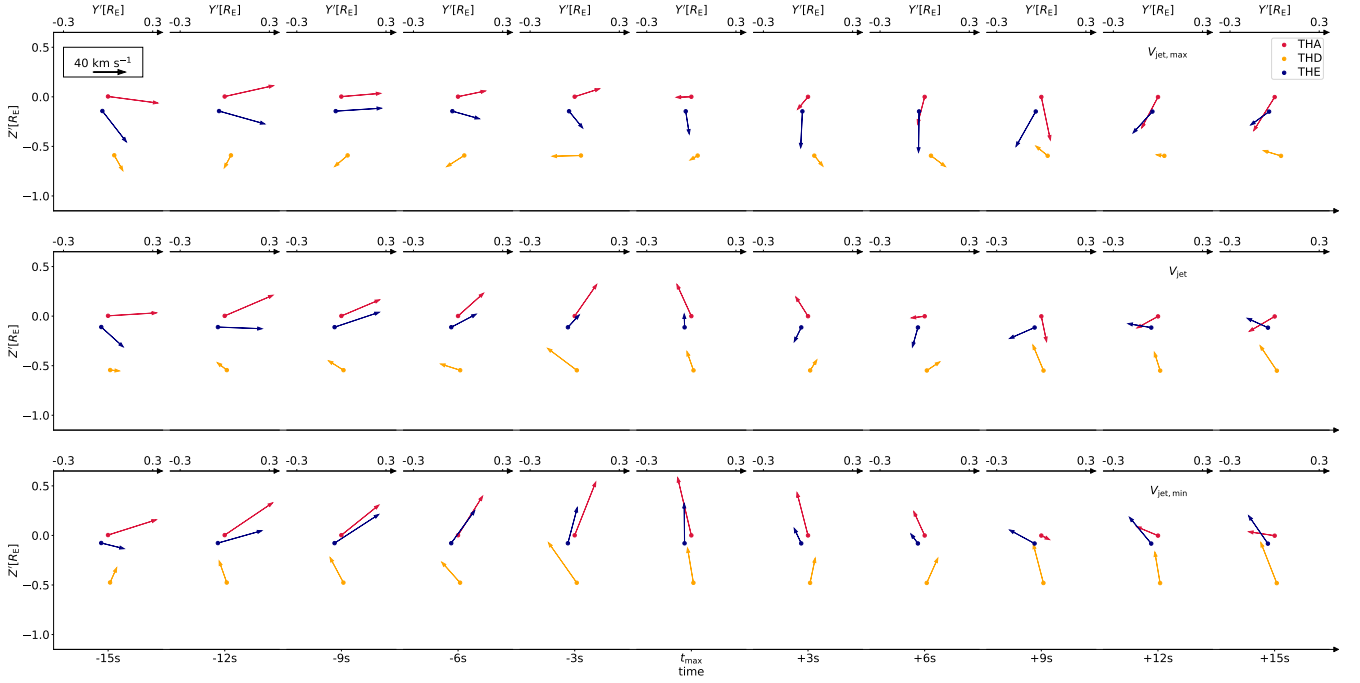
**Figure A2.** Ion velocities from the full moments at the three spacecraft positions for 11 time steps around $t_{\mathrm{max}}$ in the plane perpendicular to the jet propagation direction. The circles represent the spacecraft positions and the arrows indicate the velocities. The colors for THA, THD, and THE are red, orange, and blue, respectively. The top axes show the corresponding $\boldsymbol{Y'}$ coordinates for each time step, while the bottom axes display the time steps. In the upper left corner, the black arrow indicates the scale. The top, middle and bottom row were calculated with $\boldsymbol{V_{\mathrm{jet,max}}}$, $\boldsymbol{V_{\mathrm{jet}}}$ and $\boldsymbol{V_{\mathrm{jet,min}}}$ as propagation direction, respectively.

## Appendix B: Uncertainty of jet center estimation

Since THA and THE are close to each other and in the vicinity of the central axis in the plane perpendicular to the propagation direction, minor deviations of the position of this axis can have major effects on the dynamic pressure profiles. Therefore, we use the maximum differences from the mean to calculate alternative positions of the central axis and compare the resulting pressure profiles. In order to achieve this, we look at the fit parameters $P_0$ and $\Delta R$ and how these values change with varying central axis positions. In addition, we investigate again whether the use of the peak velocities from the 1D VDFs has a major influence on the results. Therefore, we calculate $P_{\mathrm{dyn,x}}$ from the velocities from the full moments and repeat the comparison. These results are presented in Fig. B1.

The panels (from top to bottom) show the time evolution of the fit parameters $P_0$ (a1,a2) and $\Delta R$ (b1,b2) and the time evolution of their uncertainties $\sigma(P_0)$ (c1,c2) and $\sigma(\Delta R)$ (d1,d2). The left and right column show parameters for the dynamic pressure calculated with the velocities from the 1D VDF peaks and with the velocities from the full moments, respectively.
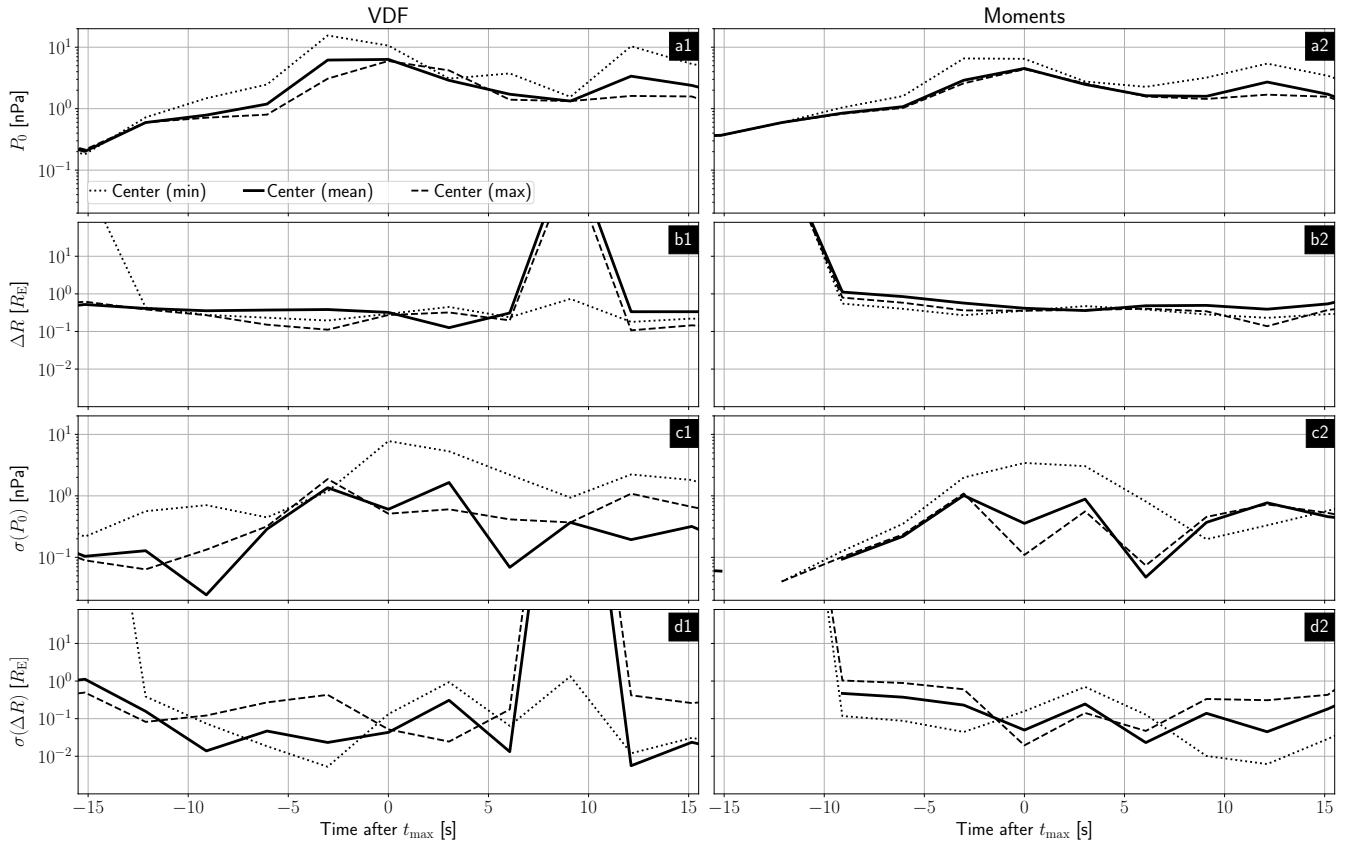
**Figure B1.** The lines represent the results with the mean central axis (solid), mean central axis with errors subtracted (dotted) and errors added (dashed). The left and right column show parameters for the dynamic pressure calculated with the velocities from the 1D VDF peaks and with the velocities from the full moments, respectively. The panels from top to bottom show the time evolution of the fit parameters $P_0$ (a1,a2) and $\Delta R$ (b1,b2) and the time evolution of their uncertainties $\sigma(P_0)$ (c1,c2) and $\sigma(\Delta R)$ (d1,d2).

The lines represent the results with the mean central axis (solid) and the mean central axis with errors subtracted/added (dotted/dashed).

The dynamic pressure at the central axis is highest around $t_{max}$ for all cases. For the subtracted errors we see an additional
270    peak later at $t_{max}$+12s. Looking at Fig. B1c, we can see that the uncertainty of the fit parameter $\sigma(P_0)$ is higher when we subtract the errors as it reduces the inter spacecraft distances.

For $\Delta R$ (Fig. B1c) we observe again a rather constant value over the whole time with some exceptions that correlate well with higher uncertainties in $\sigma(\Delta R)$ (Fig. B1d). These extremely high uncertainties arise when the data do not show a monotonic decrease in dynamic pressure and a Gaussian fit is not appropriate.
275    Apart from outliers, corresponding to high uncertainties, we observe the same behavior for the fit parameters in all cases. Therefore, we argue that the exact position of the central axis does not have a major impact on our conclusion.

*Data availability.* Data from the THEMIS mission including level 2 FGM and ESA data are publicly available from the University of California Berkeley and can be obtained from http://themis.ssl.berkeley.edu/data/themis (THEMIS, 2023). The solar wind data from NASA's OMNI high-resolution data set (1 min cadence) are also publicly available and can be obtained from https://spdf.gsfc.nasa.gov/pub/data/omni/omni_cdaweb (OMNI, 2023). THEMIS and OMNI data were accessed using the PySPEDAS software (Grimes et al., 2018; Angelopoulos et al., 2019).

*Author contributions.* AP performed the main work. GG, FK, TK, ZV and FP helped with the discussions and interpretations of the results. JM took care of THEMIS FGM calibrations and brought his expertise on THEMIS data into the discussions.

*Competing interests.* The authors declare that they have no conflict of interest.

*Acknowledgements.* We acknowledge NASA contract NAS5-02099 for use of data from the THEMIS Mission, specifically C.W. Carlson and J. P. McFadden for the use of ESA data; K. H. Glassmeier, U. Auster, and W. Baumjohann for the use of FGM data provided under the lead of the Technical University of Braunschweig and with financial support through the German Ministry for Economy and Technology and the German Center for Aviation and Space (DLR) under contract 50 OC 0302. This work was financially supported by the German Center for Aviation and Space (DLR) under contract 50 OC 2201. FK and ZV acknowledge the support by the Austrian Science Fund (FWF), P 33285-N.

# References

Angelopoulos, V.: The THEMIS Mission, Space Sci. Rev., 141, 5–34, https://doi.org/10.1007/s11214-008-9336-1, 2008.

Angelopoulos, V., Cruce, P., Drozdov, A., Grimes, E. W., Hatzigeorgiu, N., King, D. A., et al.: The Space Physics Environment Data Analysis System (SPEDAS), Space Sci. Rev., 215, 9, https://doi.org/10.1007/s11214-018-0576-4, 2019.

Archer, M. O., Horbury, T. S., and Eastwood, J. P.: Magnetosheath pressure pulses: Generation downstream of the bow shock from solar wind discontinuities, J. Geophys. Res.-Space, 117, https://doi.org/https://doi.org/10.1029/2011JA017468, 2012.

Archer, M. O., Hietala, H., Hartinger, M. D., Plaschke, F., and Angelopoulos, V.: Direct observations of a surface eigenmode of the dayside magnetopause, Nat. Commun., 10, https://doi.org/10.1038/s41467-018-08134-5, 2019.

Auster, H., Glassmeier, K., Magnes, W., andW. Baumjohann, O. A., Constantinescu, D., Fischer, D., Fornacon, K., Georgescu, E., Harvey, P., Hillenmaier, O., Kroth, R., Ludlam, M., Narita, Y., Nakamura, R., Okrafka, K., Plaschke, F., Richter, I., Schwarzl, H., Stoll, B., Vala-vanoglou, A., and Wiedemann, M.: The THEMIS Fluxgate Magnetometer, Space Sci. Rev., 141, 235–264, https://doi.org/10.1007/s11214-008-9365-9, 2008.

Balogh, A., Schwartz, S. J., Bale, S. D., Balikhin, M. A., Burgess, D., Horbury, T. S., Krasnoselskikh, V. V., Kucharek, H., Lembège, B., Lucek, E. A., Möbius, E., Scholer, M., Thomsen, M. F., and Walker, S. N.: Cluster at the Bow Shock: Introduction, Space Sci. Rev., 118, 155–160, https://doi.org/10.1007/s11214-005-3826-1, 2005.

Burch, J. L.and Moore, T. E., Torbert, R. B., and Giles, B. L.: Magnetospheric Multiscale Overview and Science Objectives, Space Sci. Rev., 199, 5–21, https://doi.org/10.1007/s11214-015-0164-9, 2016.

Dmitriev, A. V. and Suvorova, A. V.: Large-scale jets in the magnetosheath and plasma penetration across the magnetopause: THEMIS observations, J. Geophys. Res.-Space, 120, 4423–4437, https://doi.org/https://doi.org/10.1002/2014JA020953, 2015.

Dmitriev, A. V. and Suvorova, A. V.: Atmospheric Effects of Magnetosheath Jets, Atmosphere, 14, https://doi.org/10.3390/atmos14010045, 2023.

Eastwood, J. P., Lucek, E. A., Mazelle, C., Meziane, K., Narita, Y., Pickett, J., and Treumann, R. A.: The Foreshock, Space Sci. Rev., 118, 41–94, https://doi.org/10.1007/s11214-005-3824-3, 2005.

Escoubet, C., Fehringer, M., and Goldstein, M.: The Cluster mission, Ann. Geophys., 19, 1197–1200, https://doi.org/10.5194/angeo-19-1197-2001, 2001.

Grimes, E. W., Lewis, J. W., Angelopoulos, V., McTiernan, J. M., Hatzigeorgiu, N., Drozdov, A., and Russell, C.: Pyspedas, a Python Implementation of SPEDAS, in: AGU Fall Meeting Abstracts, vol. 2018, pp. IN11B–0629, 2018.

Gunell, H., Stenberg Wieser, G., Mella, M., Maggiolo, R., Nilsson, H., Darrouzet, F., Hamrin, M., Karlsson, T., Brenning, N., De Keyser, J., André, M., and Dandouras, I.: Waves in high-speed plasmoids in the magnetosheath and at the magnetopause, Ann. Geophys., 32, 991–1009, https://doi.org/10.5194/angeo-32-991-2014, 2014.

Han, D.-S., Hietala, H., Chen, X.-C., Nishimura, Y., Lyons, L. R., Liu, J.-J., Hu, H.-Q., and Yang, H.-G.: Observational proper-ties of dayside throat aurora and implications on the possible generation mechanisms, J. Geophys. Res.-Space, 122, 1853–1870, https://doi.org/https://doi.org/10.1002/2016JA023394, 2017.

Hietala, H., Laitinen, T. V., Andréeová, K., Vainio, R., Vaivads, A., Palmroth, M., Pulkkinen, T. I., Koskinen, H. E. J., Lucek, E. A., and Rème, H.: Supermagnetosonic Jets behind a Collisionless Quasiparallel Shock, Phys. Rev. Lett., 103, 245 001, https://doi.org/10.1103/PhysRevLett.103.245001, 2009.

Hietala, H., Partamies, N., Laitinen, T. V., Clausen, L. B. N., Facskó, G., Vaivads, A., Koskinen, H. E. J., Dandouras, I., Rème, H., and Lucek, E. A.: Supermagnetosonic subsolar magnetosheath jets and their effects: from the solar wind to the ionospheric convection, Ann. Geophys., 30, 33–48, https://doi.org/10.5194/angeo-30-33-2012, 2012.

330    Hietala, H., Phan, T. D., Angelopoulos, V., Oieroset, M., Archer, M. O., Karlsson, T., and Plaschke, F.: In Situ Observations of a Magnetosheath High-Speed Jet Triggering Magnetopause Reconnection, Geophys. Res. Lett., 45, 1732–1740, https://doi.org/https://doi.org/10.1002/2017GL076525, 2018.

Karlsson, T., Brenning, N., Nilsson, H., Trotignon, J.-G., Vallières, X., and Facsko, G.: Localized density enhancements in the magnetosheath: Three-dimensional morphology and possible importance for impulsive penetration, J. Geophys. Res.-Space, 117,
335    https://doi.org/https://doi.org/10.1029/2011JA017059, 2012.

Karlsson, T., Plaschke, F., Hietala, H., Archer, M., Blanco-Cano, X., Kajdič, P., Lindqvist, P.-A., Marklund, G., and Gershman, D. J.: Investigating the anatomy of magnetosheath jets – MMS observations, Ann. Geophys., 36, 655–677, https://doi.org/10.5194/angeo-36-655-2018, 2018.

King, J. H. and Papitashvili, N. E.: Solar wind spatial scales in and comparisons of hourly Wind and ACE plasma and magnetic field data, J.
340    Geophys. Res.-Space, 110, https://doi.org/https://doi.org/10.1029/2004JA010649, 2005.

Koller, F., Plaschke, F., Temmer, M., Preisser, L., Roberts, O. W., and Vörös, Z.: Magnetosheath Jet Formation Influenced by Parameters in Solar Wind Structures, J. Geophys. Res.-Space, 128, e2023JA031 339, https://doi.org/https://doi.org/10.1029/2023JA031339, 2023.

LaMoury, A. T., Hietala, H., Plaschke, F., Vuorinen, L., and Eastwood, J. P.: Solar Wind Control of Magnetosheath Jet Formation and Propagation to the Magnetopause, J. Geophys. Res.-Space, 126, e2021JA029 592, https://doi.org/https://doi.org/10.1029/2021JA029592,
345    e2021JA029592 2021JA029592, 2021.

McFadden, J., Carlson, C., Larson, D., Ludlam, M., Abiad, R., Elliott, B., Turin, P., Marckwordt, M., and Angelopoulos, V.: The THEMIS ESA Plasma Instrument and In-flight Calibration, Space Sci. Rev., 141, 277–302, https://doi.org/10.1007/s11214-008-9440-2, 2008.

Němeček, Z., Šafránková, J., Přech, L., Sibeck, D. G., Kokubun, S., and Mukai, T.: Transient flux enhancements in the magnetosheath, Geophys. Res. Lett., 25, 1273–1276, https://doi.org/https://doi.org/10.1029/98GL50873, 1998.

350    Nykyri, K., Bengtson, M., Angelopoulos, V., Nishimura, Y., and Wing, S.: Can Enhanced Flux Loading by High-Speed Jets Lead to a Substorm? Multipoint Detection of the Christmas Day Substorm Onset at 08:17 UT, 2015, J. Geophys. Res.-Space, 124, 4314–4340, https://doi.org/https://doi.org/10.1029/2018JA026357, 2019.

OMNI: Solar wind data from NASA's OMNI high resolution data set, available at: https://omniweb.gsfc.nasa.gov/ow_min.html, last access: 21 December 2023, 2023.

355    Palmroth, M., Raptis, S., Suni, J., Karlsson, T., Turc, L., Johlander, A., Ganse, U., Pfau-Kempf, Y., Blanco-Cano, X., Akhavan-Tafti, M., Battarbee, M., Dubart, M., Grandin, M., Tarvus, V., and Osmane, A.: Magnetosheath jet evolution as a function of lifetime: global hybrid-Vlasov simulations compared to MMS observations, Ann. Geophys., 39, 289–308, https://doi.org/10.5194/angeo-39-289-2021, 2021.

Plaschke, F. and Hietala, H.: Plasma flow patterns in and around magnetosheath jets, Ann. Geophys., 36, 695–703, https://doi.org/10.5194/angeo-36-695-2018, 2018.

360    Plaschke, F., Hietala, H., and Angelopoulos, V.: Anti-sunward high-speed jets in the subsolar magnetosheath, Ann. Geophys., 31, 1877–1889, https://doi.org/10.5194/angeo-31-1877-2013, 2013.

Plaschke, F., Hietala, H., Angelopoulos, V., and Nakamura, R.: Geoeffective jets impacting the magnetopause are very common, J. Geophys. Res.-Space, 121, 3240–3253, https://doi.org/https://doi.org/10.1002/2016JA022534, 2016.

Plaschke, F., Karlsson, T., Hietala, H., Archer, M., Vörös, Z., Nakamura, R., Magnes, W., Baumjohann, W., Torbert, R. B., Russell, C. T., and Giles, B. L.: Magnetosheath High-Speed Jets: Internal Structure and Interaction With Ambient Plasma, J. Geophys. Res.-Space, 122, 10,157–10,175, https://doi.org/https://doi.org/10.1002/2017JA024471, 2017.

Plaschke, F., Hietala, H., Archer, M. O., Blanco-Cano, X., Kajdič, P., Karlsson, T., Lee, S. H., Omidi, N., Palmroth, M., Roytershteyn, V., Schmid, D., Sergeev, V., and Sibeck, D.: Jets Downstream of Collisionless Shocks, Space Sci. Rev., 214, https://doi.org/10.1007/s11214-018-0516-3, 2018.

Plaschke, F., Hietala, H., and Vörös, Z.: Scale Sizes of Magnetosheath Jets, J. Geophys. Res.-Space, 125, e2020JA027 962, https://doi.org/https://doi.org/10.1029/2020JA027962, 2020a.

Plaschke, F., Jernej, M., Hietala, H., and Vuorinen, L.: On the alignment of velocity and magnetic fields within magnetosheath jets, Ann. Geophys., 38, 287–296, https://doi.org/10.5194/angeo-38-287-2020, 2020b.

Raptis, S., Karlsson, T., Plaschke, F., Kullen, A., and Lindqvist, P.-A.: Classifying Magnetosheath Jets Using MMS: Statistical Properties, J. Geophys. Res.-Space, 125, e2019JA027 754, https://doi.org/https://doi.org/10.1029/2019JA027754, e2019JA027754 10.1029/2019JA027754, 2020.

Raptis, S., Karlsson, T., Vaivads, A., Lindberg, M., Johlander, A., and Trollvik, H.: On Magnetosheath Jet Kinetic Structure and Plasma Properties, Geophysical Research Letters, 49, e2022GL100 678, https://doi.org/https://doi.org/10.1029/2022GL100678, e2022GL100678 2022GL100678, 2022a.

Raptis, S., Karlsson, T., Vaivads, A., Pollock, C., Plaschke, F., Johlander, A., Trollvik, H., and Lindqvist, P.-A.: Downstream high-speed plasma jet generation as a direct consequence of shock reformation, Nat. Commun., 13, 598, https://doi.org/10.1038/s41467-022-28110-4, 2022b.

Savin, S., Amata, E., Zelenyi, L., Lutsenko, V., Safrankova, J., Nemecek, Z., Borodkova, N., Buechner, J., Daly, P. W., Kronberg, E. A., Blecki, J., Budaev, V., Kozak, L., Skalsky, A., and Lezhen, L.: Super fast plasma streams as drivers of transient and anomalous magnetospheric dynamics, Ann. Geophys., 30, 1–7, https://doi.org/10.5194/angeo-30-1-2012, 2012.

Schwartz, S. J. and Burgess, D.: Quasi-parallel shocks: A patchwork of three-dimensional structures, Geophys. Res. Lett., 18, 373–376, https://doi.org/https://doi.org/10.1029/91GL00138, 1991.

Shue, J.-H., Chao, J.-K., Song, P., McFadden, J. P., Suvorova, A., Angelopoulos, V., Glassmeier, K. H., and Plaschke, F.: Anomalous magnetosheath flows and distorted subsolar magnetopause for radial interplanetary magnetic fields, Geophys. Res. Lett., 36, https://doi.org/https://doi.org/10.1029/2009GL039842, 2009.

Spreiter, J. R., Summers, A. L., and Alksne, A. Y.: Hydromagnetic flow around the magnetosphere, Planet. Space Sci., 14, 223–253, https://doi.org/https://doi.org/10.1016/0032-0633(66)90124-3, 1966.

Suni, J., Palmroth, M., Turc, L., Battarbee, M., Johlander, A., Tarvus, V., Alho, M., Bussov, M., Dubart, M., Ganse, U., Grandin, M., Horaites, K., Manglayev, T., Papadakis, K., Pfau-Kempf, Y., and Zhou, H.: Connection Between Foreshock Structures and the Generation of Magnetosheath Jets: Vlasiator Results, Geophys. Res. Lett., 48, e2021GL095 655, https://doi.org/https://doi.org/10.1029/2021GL095655, 2021.

THEMIS: THEMIS mission including level 2 FGM and ESA data, available at: http://themis.ssl.berkeley.edu/data/themis, last access: 21 December 2023, 2023.

Vuorinen, L., Hietala, H., and Plaschke, F.: Jets in the magnetosheath: IMF control of where they occur, Ann. Geophys., 37, 689–697, https://doi.org/10.5194/angeo-37-689-2019, 2019.

Vuorinen, L., Hietala, H., Plaschke, F., and LaMoury, A. T.: Magnetic Field in Magnetosheath Jets: A Statistical Study of BZ Near the Magnetopause, Journal of Geophysical Research: Space Physics, 126, e2021JA029 188, https://doi.org/https://doi.org/10.1029/2021JA029188, 2021.